JOURNAL OF
Materials
CHEMISTRY

Temperature-dependent structural evolution and electrochromic properties of peroxopolytungstic acid

Jin-Ho Choy,* Young-Il Kim, Joo-Byoung Yoon and Sang-Hoon Choy

National Nanohybrid Materials Laboratory, School of Chemistry & Molecular Engineering,
Seoul National University, Seoul 151-747, Korea. E-mail: jhchoy@plaza.snu.ac.kr

Received 14th November 2000, Accepted 2nd February 2001
First published as an Advance Article on the web 26th March 2001

Temperature-dependent *in situ* W L_3-edge X-ray absorption spectroscopy has been performed at 20–500 °C to investigate the geometric environment and electronic structure of tungsten upon the transformation of electrochromic peroxopolytungstic acid to tungsten trioxide. The temperature-dependent variation of the coordination number and bond distance of the nearest (W–O) sphere reveals that the peroxopolytungstate changes into crystalline tungsten oxide through the gradual removal of peroxo species, zeolitic water, hydroxyl groups, and terminal W=O bonds, which is also confirmed by thermal analysis, powder XRD, and FT-IR spectroscopy. It is especially emphasized that the intermediate structure of peroxopolytungstate at 120–200 °C is characterized by a substantial number of oxygen vacancies together with a partially formed oxide lattice. A thin film of peroxopolytungstic acid has been prepared on a transparent conducting substrate and post-annealed at 100–300 °C. From cyclic voltammetry and optical density measurements in a $LiClO_4$–propylene carbonate electrolyte, it was found that the voltammetric exchange charges are maximized for films annealed at 150–200 °C, whereas the voltage response of coloration/bleaching is depressed by the increase in annealing temperature. Considering both the electrochromic kinetics and redox capacity, the optimum annealing temperature for the formation of WO_3 film was determined to be 120–200 °C. Such results could be well explained in terms of the structural evolution of peroxopolytungstic acid on the basis of X-ray absorption spectroscopic analysis.

Introduction

Owing to its versatile electronic, structural, and electrochemi-optical properties, tungsten polyacid and related systems have been widely studied with a view towards potential applications in electrochromics,[1–5] catalysis,[6,7] and inorganic resistors,[8] *etc.* In particular, the above polytungstates have been frequently used as precursors in preparing thin films on various types of substrates by spin- or dip-coatings which are advantageous in terms of fabrication cost and time compared to conventional vacuum deposition methods such as sputtering or evaporation. In those wet chemical coatings, post-annealing is often performed to control the film's composition, microstructure, and, ultimately, its reactivity and stability. Therefore, it is very important to characterize the intermediate phases formed during the transformation from the precursor sol to the crystalline phase of the coating material, not only for achieving the desired performance but also for understanding the engaging mechanism. For example, the peroxopolytungstate (WPA) derived WO_3 film is well known to exhibit the electrochromic effect, a reversible change in the optical absorption coefficient upon electrochemical redox switching which is typically the cation (H^+, Li^+, Na^+, or K^+) intercalation. In the electrochromic process of WO_3, the coloration efficiency, reversibility, and long-term reproducibility are greatly dependent on the internal structure and grain morphology of the film. Considering the two key criteria for electrochromics, namely coloration kinetics and durability, the optimum annealing conditions for WO_3 films have been estimated as 100 °C for 1 h and ~200 °C for 30 min.[9,10] However, for the above thermal conditions, the structural evolution of WPA is not explained clearly enough to suggest a correlation between the annealing temperature of the WO_3 film and its electrochemical behavior. This is mainly because the precursor WPA remains amorphous up to 350 °C, which prevents the application of conventional tools such as X-ray diffraction (XRD) and infrared (IR) and Raman spectroscopies. Although it has been reported that two crystalline WPA phases are formed during the drying process of peroxopolytungstic acid solution, they can be obtained only under very mild conditions ($\leqslant$120 °C).[11] IR and Raman spectroscopic studies are frequently used for the identification of specific chemical groups, but they are generally inadequate for probing an unknown structure. A previous XRD study using the radial distribution function (RDF) has proposed that WPA consists of a structural unit based on paratungstate-B, $[W_{12}O_{42}H_2]^{10-}$, and maintains a 2-dimensional pyrochlore structure up to 200 °C.[1] However, the RDF found by the diffraction method is a single averaged function accounting for all the elements present, and therefore the data analysis is not straightforward.[12]

In this regard, X-ray absorption spectroscopy (XAS) can be very effective for resolving the structure of WPA, since the extended X-ray absorption fine structure (EXAFS) enables quantitative structural determination by extracting a partial RDF for each element by tuning the X-ray energy to a specific absorption edge. EXAFS spectroscopy is equally suitable for non-crystalline as well as crystalline material and is applicable to various physical states including gas, liquid, and solid.[12–15] In addition, the W L_3-edge X-ray absorption near edge structure (XANES) spectroscopy can provide information on the electronic structure and chemical bonding nature of tungsten which closely reflects the shape of the W–O bonding sphere.[16] In the present study, we have investigated the structural evolution of WPA upon heating, with *in situ* XAS at the W L_3-edge. Using the XAS results for WPA at 20–500 °C along with powder XRD, thermogravimetry/differential thermal analysis (TG/DTA), and IR spectroscopy, it is demonstrated how the electrochromic property of WO_3 film is influenced by the local structure around the electrochromic center.

Experimental

Preparation and characterization of WPA

To prepare the WPA xerogel 15 g of tungsten metal powder (particle size ~1 μm) were slowly added to 50 ml of 15% H_2O_2 solution placed in an ice bath. After being kept at room temperature for 24 h, the solution was filtered and dried at reduced pressure ($\sim 10^{-2}$ Torr) to yield a light-yellow glassy solid.[1] TG/DTA were carried out in air at a heating rate of $10\,^{\circ}C\,min^{-1}$ between 20–600 °C by using a Rigaku TAS-100 system. Iodometric titration was carried out to determine the peroxide content. Powder XRD data were collected with a Philips X-ray diffractometer (PW1830) equipped with Ni-filtered Cu-Kα radiation ($\lambda = 1.5405$ Å). Fourier transform infrared (FT-IR) spectra were recorded as KBr pellets on a Perkin-Elmer Spectrum 2000 Explorer.

W L_3-edge X-ray absorption spectroscopy

The temperature-dependent W L_3-edge XANES and EXAFS spectra were taken at the BL 10B station of Photon Factory, Tsukuba, operating at 2.5 GeV with a stored ring current of 350–400 mA. The Si(311) channel-cut monochromator was used, and the intensities of the incident and transmitted beams were measured with ionization chambers filled with N_2/Ar (v/v = 85/15) mixture gas. For the measurement on WPA solution, 10 wt% aqueous solution was placed in a cell (path length = 6 mm) with Kapton windows. The powder sample was prepared as a pellet mixed with boron nitride and placed at the electrical furnace. The temperature-dependent measurements were carried out after a retention period of 30 min at each temperature (heating rate = $10\,^{\circ}C\,min^{-1}$). During the measurements, the thickness effect was carefully checked and removed by fine-tuning the pellet thickness.

XANES and EXAFS data analyses were performed using standard procedures.[13,14,17] For XANES, the inherent background in the data was extracted by fitting a polynomial to the pre-edge region and extrapolating through the entire spectrum. After background subtraction, the resulting spectrum, $\mu(E)$, was normalized to an edge jump of unity for comparing the XANES features directly. All the present spectra were calibrated by the maximum of the first derivative XANES spectrum of WO_3. In order to obtain more detailed information on the electronic state and local symmetry around tungsten, a deconvolution method was applied to the XANES spectra using two Lorentzian functions (corresponding to transitions to the t_{2g} and e_g levels) and one arc tangent (corresponding to the transition to the continuum level).[16,17]

For EXAFS data analysis, the absorption spectrum for the isolated atom, $\mu_0(E)$, was approximated by a cubic spline function, and the EXAFS, $\chi(E)$, was obtained as $\chi(E) = \{\mu(E) - \mu_0(E)\}/\mu_0(E)$. Further analysis was performed in k-space, where the photoelectron wave vector is defined as $k = \{(2m_e/\hbar^2)(E - E_0)\}^{1/2}$, where m_e is the electron mass and E_0 is the threshold energy of photoelectrons at $k = 0$. The resulting EXAFS spectra were k^3-weighted and Fourier-transformed in the range $3.5 \leqslant k(\text{Å}^{-1}) \leqslant 13.5$ with a Hanning apodization function to reduce the truncation effect. In order to determine structural parameters around tungsten, non-linear least-squares curve fitting was carried out for the first shell corresponding to the W–O bonding pair in R-space by using the software UWXAFS2[18,19] based on the following EXAFS formula:

$$\chi(k) = S_0^2 \Sigma_i N_i(k) \exp\{-2\sigma_i^2 k^2 - 2R_i/\lambda(k)\}$$
$$\sin\{2kR_i + \phi_i(k)\}/(kR_i^2)$$

The back-scattering amplitude, $F_i(k)$, the total phase shift, $\phi_i(k)$, and the photoelectron mean free path, $\lambda(k)$, have been theoretically calculated for all scattering paths by the curved wave *ab initio* EXAFS code FEFF6.[20–22] Monoclinic WO_3,[23] tetravalent WO_2, $SrWO_4$, and $WO_3 \cdot H_2O$[24] were used as reference compounds, and throughout the entire fitting procedure, the amplitude reduction factor ($S_0{}^2$) for the W–O bond was set equal to 0.85, as obtained from WO_3. In the course of non-linear least-squares curve fitting between the experimental spectrum and the theoretical counterpart, structural parameters such as bond distance (R_i), coordination number (N_i), Debye–Waller factor ($\sigma_i{}^2$), and threshold energy difference (ΔE_0) were determined.

WO_3 film coating and electrochromic properties

Tungsten oxide film was prepared by spin-coating the WPA solution on a transparent conducting substrate, In_2O_3–Sn (ITO). The coating solution, obtained by dissolving WPA in an EtOH–H_2O mixture (v/v = 50/50) with a concentration of $500\,mg\,ml^{-1}$, was spun onto the ITO-coated glass (Samsung Corning, $12\,\Omega\,\square^{-1}$) at 1800 rpm for 30 s, using a commercial photo-resist spinner (Headway Research, PM101-CB15). The as-coated film was cut into six pieces, each of which was heated for 30 min at different annealing temperatures of 100, 120, 150, 200, 250, and 300 °C. The thickness of each as-annealed WO_3 layer was measured with a surface profiler (Taylor Hobson, Talystep). In order to estimate the density and compactness of each WO_3 film, thickness measurement was also performed for a film treated at 450 °C.

For the WO_3 films obtained at different annealing temperature (τ_a), cyclic voltammetry was carried out in the potential (E) range −1.0 V to +1.0 V (*versus* Ag/AgCl) with a sweep rate of $5\,mV\,s^{-1}$. The three-electrode system was constructed using Pt wire and Ag/AgCl with a Luggin capillary as the counter and the reference electrode, respectively, and the electrolyte was 1.0 M $LiClO_4$ dissolved in propylene carbonate. The electrochromic behavior of WO_3 film was examined under potentiostatic conditions, in a quartz cell compartment of a spectrophotometer (Perkin-Elmer, Lambda 12). For the coloration/bleaching of WO_3 film, double step voltages of −2.2 V (10 s)/+3.0 V (25 s) and −3.0 V (10 s)/+3.3 V (25 s) were applied between WO_3 and Pt electrodes. The transmittance (T) of WO_3 film was monitored at a fixed wavelength of 550 nm, and the optical density (ΔOD) was determined as log ($T_{bleached}/T_{colored}$). During the above electrochromic processes, chronoamperometry was also carried out to estimate the amount of intercalated Li. All the electrochemical and electrochemi-optical measurements were performed using an automatically controlled potentiostat/galvanostat (Arbin, BTS-2040).

Results and discussion

TG, XRD and FT-IR

WPA is formed with various compositions of $WO_3 \cdot nH_2O_2 \cdot mH_2O$ or $WO_{3-n} \cdot (O_2)_n \cdot mH_2O$ depending on the preparation conditions,[1,9] and the values n and m can be determined by TG and iodometry. The TG of WPA (Fig. 1a) shows weight changes in two steps at 20–200 °C (13.8 %) and 200–350 °C (2.8%), respectively, and its first derivation indicates that each step consists of several different types of reactions. The weight decrease in the first step is mainly due to the decomposition of peroxo species at ~90 °C and to the desorption of the surface water at ~140 °C, as confirmed by IR

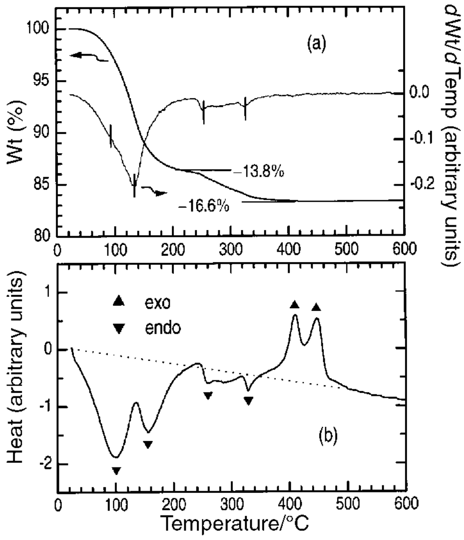

Fig. 1 Thermal analysis profiles of WPA: (a) thermogravimetry (thick line) and its first derivative (thin line), and (b) differential thermal analysis. The sample was heated at a rate of 10 °C min^{-1} in air.

studies (discussed below). At 200–350 °C, the hydroxyl groups and water molecules, which are strongly coordinated to tungsten in WPA, are released. In the DTA curve (Fig. 1b), four endothermic peaks can be observed, consistent with the TG result with some additional exothermic peaks indicating the crystallization to monoclinic WO_3 (~410 °C) and its transition to the orthorhombic phase (~450 °C).[25] The peroxide content within WPA was determined by iodometric titration, and subsequently the composition of the as-prepared WPA could be approximated as $WO_3{\cdot}1.0H_2O_2{\cdot}1.5H_2O$.

The XRD patterns shown in Fig. 2 were measured at room temperature after the heat treatment of WPA at the indicated temperature for 30 min. For the as-prepared WPA, several sharp diffraction peaks are observed corresponding to the tungsten oxide peroxide hydrate (PDF No. 43–0698), but the overall XRD pattern is dominated by broad features due to the amorphous nature of the main phase. After heat treatment at 120 °C, the diffraction lines of the hydrate mostly disappear, and remain as weak traces only. And for the samples treated at 200 and 350 °C, no discernible diffraction line could be detected except for the peak growth at $2\theta \approx 23°$. The crystallization of tungsten oxide becomes significant beyond 420 °C, and complete at 450 °C.

The FT-IR spectra (Fig. 3) were also measured for the same samples used in the XRD study. The as-prepared WPA shows absorption bands corresponding to $W{=}(O_2)$ (550 cm^{-1}),[26] bridging peroxide (880 cm^{-1}), terminal W=O (960 cm^{-1}), and hydroxyl group (1620 cm^{-1}), together with the band due to W–O stretching vibrations of crystalline WO_3 (~650 cm^{-1}).[27] This result suggests that the as-prepared WPA is composed of various structural units of W–O–W, W=O, W–O–O–W, $W{=}(O_2)$, $W{-}OH_2$, *etc.* The peroxide species are decomposed below 200 °C, while the W=O and hydroxyl components can be detected even at 300 and 350 °C, respectively. The sample treated at 450 °C gives almost the same spectra as that of monoclinic tungsten oxide, which is the room temperature isomorph of stoichiometric WO_3.[28]

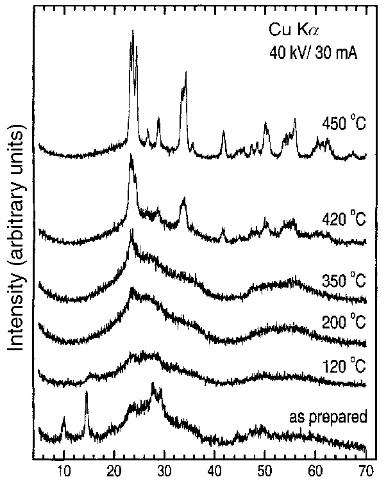

Fig. 2 Powder XRD patterns for the WPA, depending on the heat treatment conditions.

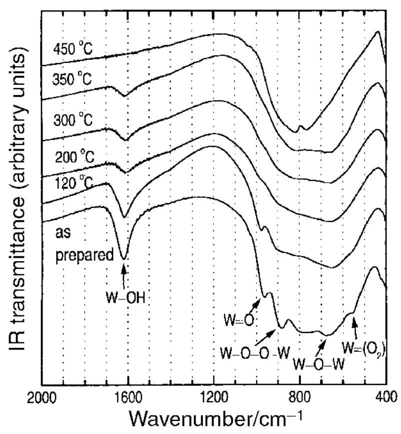

Fig. 3 FT-IR spectra for the WPA, depending on the heat treatment conditions.

W L_3-edge X-ray absorption spectroscopy

The XAS technique was used to investigate the temperature-dependent evolution of local structure around W and the W–O bonding character in WPA. From the deconvolution analysis of the XANES spectra, the peak position (*E*), amplitude (*H*), and full-width-at-half-maximum (Γ) could be determined for each of the transitions to the t_{2g} and e_g levels, as given in Fig. 4 and Table 1. For all the spectra for WPAs, the shapes and positions of the absorption edges are very close to those for WO_3, implying that the tungsten ions exist as W^{6+} with octahedral symmetry. Nevertheless the variation of white line (WL) intensity indicates that the WO_6 octahedron is considerably distorted for samples at lower temperatures. The tungstate in the WPA solution can be depicted as a molecular cluster, and therefore, the sharp and intense WL peak is attributed to its narrower d-band structure compared to the crystalline phase. Its WL amplitude and the summed areas for vacant t_{2g} and e_g bands are ~25% larger than those for the others. In general, the WL area is directly related to the 5d vacancy or the oxidation number of the absorbing ion but in the present case it is hard to predict the variation of the W 5d vacancy since the oxidation state of tungsten is commonly $W^{6+}(5d^0)$ in all the samples. Instead, the unusual WL feature of the WPA solution might be due to the covalency of the short and strong W=O bond, which was similarly observed for the hydrated WO_3 system.[29,30] Beyond 200 °C, the WL amplitude remains nearly the same, whereas Γ becomes larger as the temperature increases due to the d-band broadening by oxide network formation. Since the energy gap (ΔE) between the t_{2g} and e_g levels for WO_6 symmetry is obviously differentiated from that between the t and e_2 levels for WO_4 symmetry, it can be an indicator of tetrahedral (T_d) or distorted octahedral (O_h) fractions within WPA. For $SrWO_4$ and WO_3, the ΔE's were 2.3 and 3.72 eV, respectively, and for WPA, it increases monotonically from 2.8 to 3.71 eV along with the measurement temperature. This implies that the crystallization of tungsten

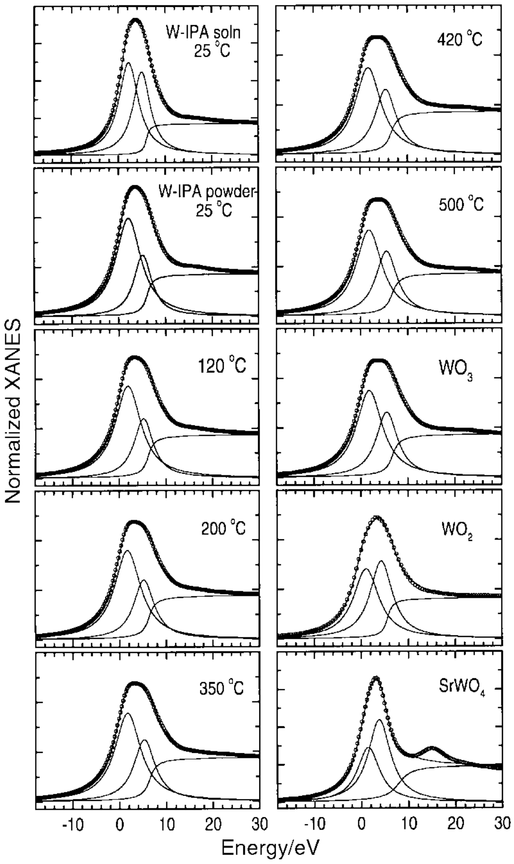

Fig. 4 Curve-fitting results for XANES of the WPA in aqueous solution and the salt at 20–500 °C, and those of references, WO$_3$, WO$_2$, and SrWO$_4$.

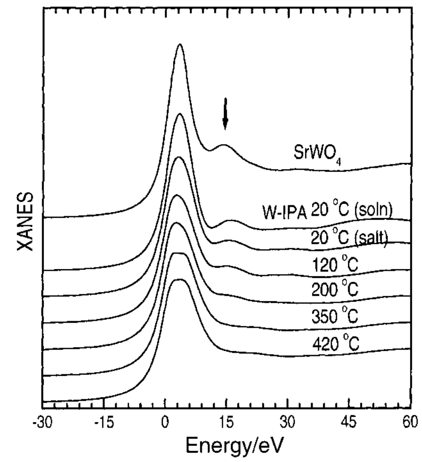

Fig. 5 Comparison between the normalized XANES spectrum of SrWO$_4$ and the modified XANES spectra for WPA (see the text) at 20 °C (solution and salt), 120 °C, 200 °C, 350 °C and 420 °C.

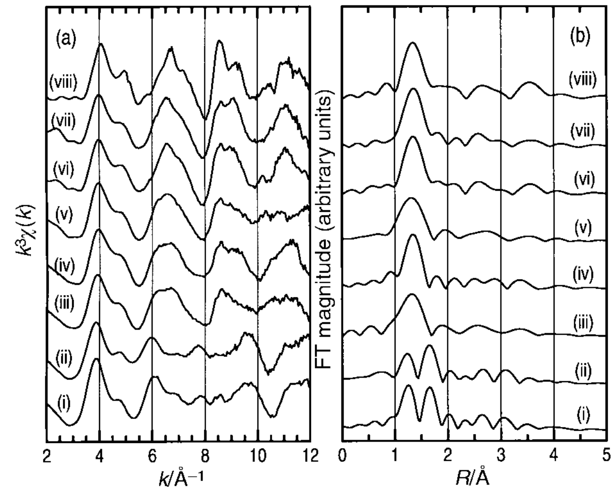

Fig. 6 (a) k^3-Weighted W L$_3$-edge EXAFS spectra and (b) their Fourier transforms for the WPA samples and reference WO$_3$: (i) WPA solution, and WPA salt at (ii) 20 °C, (iii) 120 °C, (iv) 200 °C, (v) 350 °C, (vi) 420 °C, (vii) 500 °C, and (viii) WO$_3$.

oxide is not complete up to 350 °C and moreover there are significant T_d characteristics in the samples below 200 °C due to the severe oxygen defect or local distortion around tungsten. The fitting results for the XANES spectra at 420 °C and 500 °C are similar to those for the reference WO$_3$, where the energy difference (ΔE), area ratio ($A_{t_{2g}}/A_{e_g}$), and total area (A_{tot}) are very close to those for regular local octahedral symmetry.

As an alternative means of estimating the presence of the T_d character in WPA due to the octahedral defect or local distortion around tungsten, the XANES spectra for 20–420 °C were processed as follows. From each X-ray absorption spectrum for WPAs, 0.7-weighted data for 500 °C was subtracted and then normalization was performed again through which the near edge features could be emphasized. In Fig. 5, the modified spectra of WPA are presented together with the XANES spectrum of SrWO$_4$. Owing to the tetrahedral component of WO$_4^{2-}$, the SrWO$_4$ spectrum exhibits a prominent peak at ~15 eV above the absorption edge,[30] and similar features can be observed also in the modified spectra of WPA at lower measurement temperatures. The above characteristics have completely disappeared at ⩾350 °C, but the samples at 120–200 °C are thought to contain substantial amounts of the T_d species due to the highly distorted octahedra or oxygen defects in WPA. The samples heat treated at 120–

Table 1 The Lorentzian parameters for the normalized XANES spectra obtained from the curve-fitting[b]

		WPA											
O_h (WO$_6$)		Soln.	20 °C	120 °C	200 °C	350 °C	420 °C	500 °C	WO$_3$	WO$_2$	T_d (WO$_4$)		SrWO$_4$
t$_{2g}$	H	2.49	1.98	1.86	1.79	1.78	1.75	1.73	1.75	1.41	e	H	1.45
	Γ	5.16	6.54	6.76	6.80	6.76	6.73	6.74	6.75	6.54		Γ	5.68
	E	2.07	2.10	1.85	1.75	1.70	1.69	1.84	1.84	1.06		E	1.88
e$_g$	H	2.24	1.24	1.20	1.20	1.24	1.31	1.30	1.32	1.57	t$_2$	H	2.19
	Γ	4.52	4.64	5.00	5.32	5.50	5.53	5.58	5.54	5.70		Γ	5.80
	E	4.86	5.16	5.19	5.22	5.27	5.40	5.55	5.56	4.28		E	4.21
A_{tot}[c]		36.1	29.4	29.2	29.1	29.6	29.9	29.7	30.1	28.6	A_{tot}[c]		32.9
$A_{e_g}/A_{t_{2g}}$		0.79	0.44	0.48	0.52	0.57	0.62	0.62	0.62	0.97	A_{t_2}/A_e		1.54
$E_{e_g}-E_{t_{2g}}$		2.79	3.06	3.34	3.47	3.57	3.71	3.71	3.72	3.22	$E_{t_2}-E_e$		2.33

[a] Amplitude (H) is expressed in normalized XANES units, full-width-at-half-maximum (Γ) and energy (E) are in eV, and the area (A) is in (XANES unit × eV). [b] Errors in E and Γ are ±0.05 eV, and in H, ±0.05 units. [c] Sums of the peak areas for the two Lorentzian functions corresponding to t$_{2g}$ and e$_g$ transitions for O_h symmetry and that corresponding to e and t$_2$ for T_d, respectively.

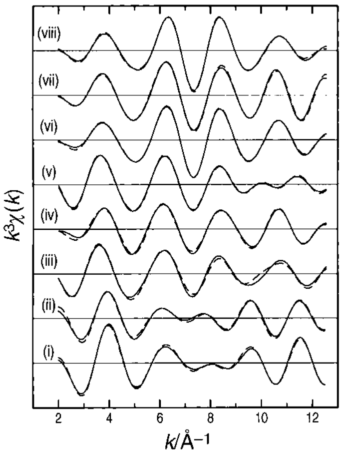

Fig. 7 Best-fit profiles of the inverse Fourier transformed EXAFS spectra for the WPA solution (i) and salt at (ii) 20 °C, (iii) 120 °C, (iv) 200 °C, (v) 350 °C, (vi) 420 °C, (vii) 500 °C, and (viii) that for the reference WO_3 (Experimental: solid lines, calculated: dashed lines).

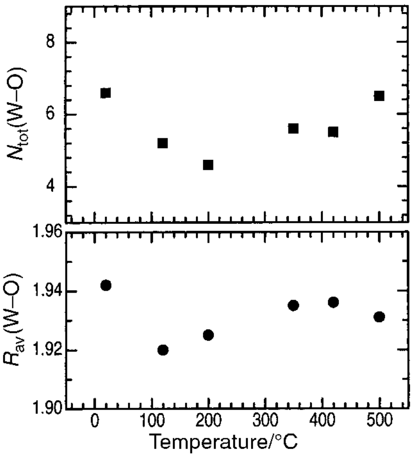

Fig. 8 Temperature-dependent variation of (top) N_{tot} and (bottom) R_{av} for the nearest (W–O) coordination sphere in WPA.

200 °C may form such defect structures since the coordinated water ligands are mostly liberated as demonstrated in the TG/DTA result, while the polymerization of tungstic acid is as yet incomplete in that temperature range.

Fig. 6 shows the k^3-weighted W L_3-edge EXAFS spectra for WPA at different temperature points and their Fourier transforms (FT). In the FT spectra, the peaks at $R < 2$ Å (without the phase-shift correction) originate from the single scattering EXAFS for the tungsten atom. Particularly, the room temperature samples show two well separated peaks in that region due to the significant contribution from short W=O bonds as well as that from long W–(OH_2) bonds. In order to filter the structural information on the nearest tungsten–oxygen bonding sphere, each FT spectrum was inverse Fourier transformed in an appropriate R-space range, to which non-linear least-squares curve fitting was applied. The best-fit profiles and the fitting parameters are given in Fig. 7 and Table 2, respectively.

Table 2 Structural parameters for the W–O bonds in WPA at various temperatures determined from the W L_3-edge EXAFS analysis[a]

Sample	N_i[b]	R_i/Å	10^{-3} σ_i^2/Å^2	E_0/eV	N_{tot}[c]	R_{av}[d]
WPA solution at 20 °C	1.1	1.70_4	1.1			
	5.2	1.93_0	12.3	3.82	7.3	1.93_7
	1.0	2.23_0	3.8			
WPA salt at 20 °C	1.4	1.70_6	3.9			
	4.2	1.94_9	10.3	3.01	6.6	1.94_2
	1.0	2.24_7	5.6			
120 °C	2.5	1.77_3	4.6			
	1.6	1.97_9	2.3	5.22	5.2	1.92_0
	1.1	2.16_9	2.3			
200 °C	1.8	1.75_6	2.1			
	1.7	1.94_8	5.3	5.83	4.6	1.92_5
	1.1	2.16_5	8.4			
350 °C	1.9	1.72_0	2.5			
	1.7	1.97_9	1.2	3.42	5.6	1.93_5
	2.0	2.10_1	6.9			
420 °C	2.4	1.75_6	2.3			
	1.1	1.95_4	1.9	3.44	5.5	1.93_6
	2.0	2.14_3	4.7			
500 °C	3.1	1.77_0	5.2			
	2.6	2.04_2	5.4	3.75	6.5	1.93_1
	0.8	2.19_8	2.0			
WO_3 (monoclinic)	2.0	1.74_1	1.9			
	2.0	1.93_1	6.8	5.36	6.0	1.94_1
	2.0	2.15_2	4.0			

[a] The fitting accuracy is about 0.01 Å for the bond distance (R_i), and 25% for the coordination number (N_i) and Debye–Waller factor (σ_i^2). [b] N_i was evaluated using the amplitude reduction factor of reference WO_3 (0.85). [c] Total coordination number. [d] Average bond distance.

The as-prepared WPA and its aqueous solution were found to have similar W–O bond lengths and coordination numbers as expected from their EXAFS oscillations and FTs. The refined parameters for both samples are quite consistent with the previous structure model for WPA based on the RDF method.[1] Although these two samples show slight differences in R_i, N_i, and σ_i^2, they seem to possess very similar framework structures in which the isolated polytungstates interface with H_2O molecules through weak electrostatic interaction. Such a weak coordination by surface oxygen to the tungsten is well expressed by the decrease of R_i and σ_i^2 parameters for the competing W=O bond, and also by the prominent WL intensities of the corresponding XANES spectra.

For the samples beyond 120 °C, the total coordination number (N_{tot}) of the oxygen shell was found to decrease remarkably, which is in accordance with the fact that WPA gradually releases H_2O and O_2^{2-} as the temperature is raised. Comparing the refined EXAFS data for the sample at 120 °C with that at 20 °C, it was found that the removal of H_2O/O_2^{2-} results not only in the decrease of N_i at 1.95–2.0 Å but also in the increase of N_i at 1.7–1.8 Å. On the other hand, no noticeable structural evolution of WPA could be observed between 120 and 200 °C, except for the reduction of N_i for the shortest W=O bond. These findings indicate that terminal W=O bonds are simultaneously formed during the dehydration/deoxygenation from WPA for the charge compensation (at <120 °C) and they are partially converted to bridging oxygens which initiate –W–O–W– network formation (at 120–200 °C). Further heat treatment of WPA led to a gradual transformation to the stoichiometric and crystalline WO_3 phase with orthorhombic symmetry,[31] which was confirmed by EXAFS analysis for the data obtained at 500 °C.

Since the electrochromic function of WO_3 film is strongly influenced by its microstructure, for example by factors such as the availability of favorable sites and diffusion paths for the Li^+/H^+ ions, the EXAFS analysis of WPA can be useful for explaining the annealing-dependent electrochromic property of the WO_3 films. The EXAFS results for WPA are summarized in the plots in Fig. 8, which show that both total coordination number, N_{tot}, and average bond distance, R_{av}, for the nearest (W–O) shell are minimized at 120–200 °C. This means that the intermediate phase of WPA treated at 120–200 °C is quite rich in the terminal W=O bonds and incomplete WO_6 octahedra, although its internal oxide network is almost complete. Therefore, we propose a model structure that might be found during the structural evolution of WPA as given in Fig. 9. The as-prepared WPA can be described as a phase with

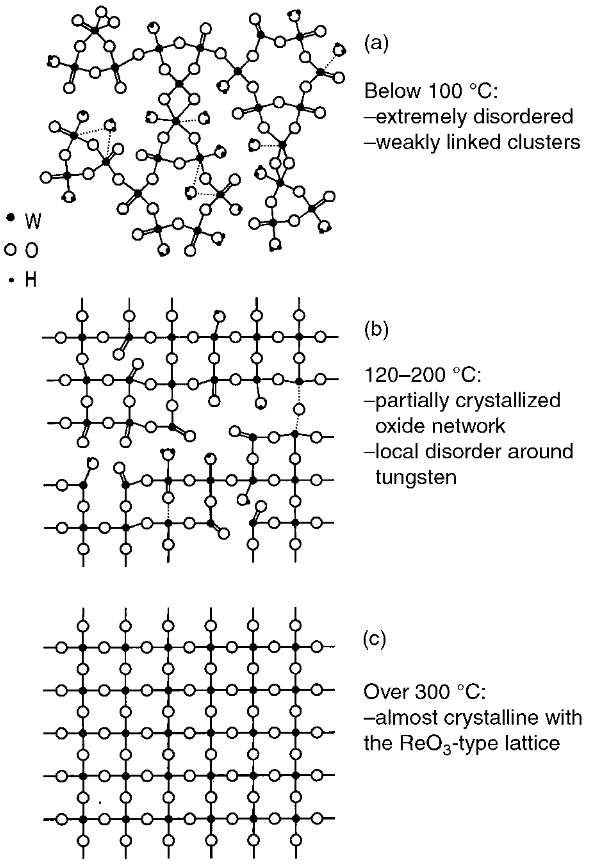

Fig. 9 Models for the structural evolution from amorphous WPA to crystalline WO_3, where the crystallization proceeds from (a) to (c). For clarity, the structures are described only in two dimensions.

an amorphous xerogel structure consisting of weakly cross-linked tungstate oligomers. Upon heating, it releases sub-components such as H_2O and O_2^{2-}, and then begins to crystallize into the corner-sharing array of WO_6 octahedra. During the transformation from an extremely amorphous state (Fig. 9a) to a completely crystalline one (Fig. 9c), WPA should be formed with the structure suggested in Fig. 9b. It should be noted that the microstructure of Fig. 9b can be effective for the Li^+ intercalation in both the electrochemical kinetics and the redox capacity, since it provides sufficient and easily accessible lithiation sites. It is therefore understood that the structural defects in the WPA based film are properly controlled at 120–200 °C in such a way that its electrochromic function can be optimized.

Electrochromic properties of WO_3 film

In order to investigate the dependence of the electrochromic property on annealing temperature based on the above structural information, WPA films were prepared by the spin-coating method. The thickness (t) of the spin-coated WO_3 film was measured with a surface profiler after heat-treatment. Although the present films have been prepared by the same procedure except for the annealing temperature (τ_a), their thickness values were changed significantly from 240 ± 10 nm ($\tau_a = 100$ °C) to 145 ± 8 nm ($\tau_a = 300$ °C). As can be predicted from the TG profile of WPA, the film undergoes dehydration and deoxygenation at 100–300 °C, resulting in a notable shrinkage of the thickness. In particular, the film with $\tau_a = 300$ °C has a very similar thickness to that of the crystalline phase ($\tau_a = 50$ °C) and it is therefore assumed that a highly dense network of WO_3 is formed.

The electrochemical and electrochromic properties of the WO_3 film derived from WPA have been examined by cyclic voltammetry and optical density measurement under potentiostatic conditions. Fig. 10 shows the voltammetry profile for 10 successive cycles, which was measured for each as-annealed film at a given temperature. As revealed by the evolution of the voltammograms, all the present samples underwent pronounced surface curing that is a general characteristic of sol–gel produced film.[32] Such irreversible reductions can be ascribed mainly to two kinds of reactions: decomposition of H_2O, O_2^{2-} or O^- (dominant in the films with low τ_a) and irreversible lithiation at the terminal W=O site (dominant in the films with high τ_a). During the repeated redox cycles, all the samples showed reversible color changes between intense blue at the cathodic limit and colorless at the anodic limit. For six samples, the degree of coloration was similar, with a maximum ΔOD of 0.4–0.5 at $\lambda = 550$ nm but the kinetics of the coloration/bleaching were quite distinct depending on τ_a. From the voltammetry curves, it can be noted that the elevation of τ_a accompanies a negative shift of the coloration onset potential as well as a positive shift of the end-point of bleaching. It means that both the Li^+ intercalation and deintercalation are depressed by the elevation of τ_a from 100 °C to higher temperature points. Taking into account the variation of the WO_3 film thickness as a function τ_a, it is obvious that τ_a influences the microstructure of each film and consequently its electrochemical properties. For instance, it is assumed that a sample with $\tau_a = 300$ °C ($t = 145$ nm) is much denser than one with $\tau_a = 100$ °C ($t = 240$ nm), which must be very porous with a density as low as ~60% of that found in crystalline WO_3. This implies that the Li^+ intercalation can occur *via* different paths depending on the extent of annealing and crystallization of the host film. In the WO_3 films with lower τ_a, the grain boundary can serve as a facile channel for Li^+ diffusion;[2] on the other hand, in those with higher τ_a, Li^+ should penetrate into the dense WO_3 grain suffering from a much higher activation barrier. In cases with τ_a's of 120, 150, and 200 °C, the evolution of the voltammograms indicates that the reactivity of each film is gradually improved, which is probably due to the modifica-

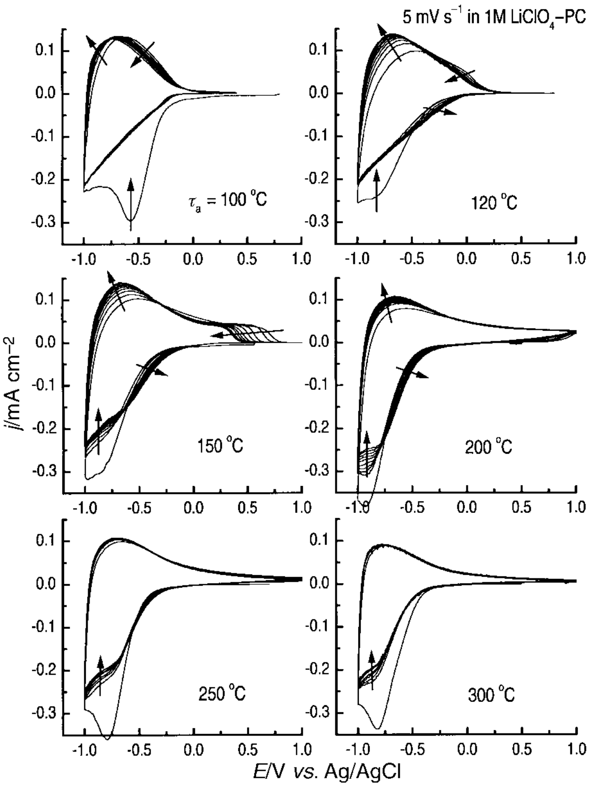

Fig. 10 Cyclic voltammograms measured for the as-annealed WO_3 films. Arrows indicate the propagation of voltammograms along the cycles.

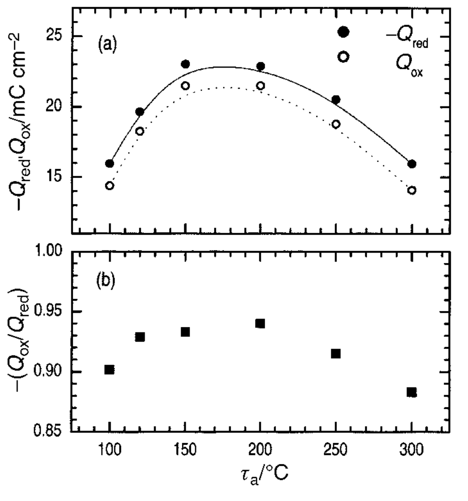

Fig. 11 (a) Exchange charges during the reduction ($-Q_{red}$) and oxidation (Q_{ox}), and (b) the ratio of Q_{ox} to $-Q_{red}$, calculated for the 50th redox cycle of each film.

tion of internal microstructure. It is therefore thought that these films ($\tau_a = 120$, 150, and 200 °C) consist of a partially crystallized moiety as well as an amorphous moiety, in which the former can be readily transformed into an efficient diffusion path for Li^+ ions.

In addition to the intercalation kinetics, the charge capacity (between -1.0 and $+1.0$ V *vs.* Ag/AgCl) of each film is also found to vary depending on the annealing conditions, as depicted in Fig. 11. For the 50th redox cycle of each film, in which the voltammogram became almost reproducible, the exchange charges during reduction ($-Q_{red}$) and oxidation (Q_{ox}) and also their ratio, $-(Q_{ox}/Q_{red})$, are shown to be maximized for τ_a's between 150 and 200 °C. Since the six samples were prepared to have the same area density of tungsten, the different Li^+ capacities are attributed to structural properties such as porosity and grain size. As mentioned above, the films with τ_a's around 150 °C can provide sufficient and easily accessible redox sites not only in the grain surface but also in the internal space of the grains. Such an intermediate crystallinity is regarded to be well suited for the accommodation of Li^+ ions, though it is slightly inferior from the viewpoint of Li^+ diffusion rate. For the two opposite cases of $\tau_a = 100$ °C and 300 °C, the poor capacities can be explained by distinct causes. In the former, the lithiation sites are provided exclusively at the grain surface due to the incomplete growth of the tungsten oxide network, and therefore they are apt to be saturated with a low Li/W ratio. On the other hand, the film with $\tau_a = 300$ °C possesses a more close-packed ReO_3-type lattice with abundant vacancies available for Li^+ insertion but these vacancies are located deep inside the crystallized grains and seem to be only partially filled under voltammetric conditions.

The electrochromic properties of WO_3 films have been investigated by chronoamperometry and *in situ* ΔOD measurement in which voltage steps of (-2.2 V/$+3.0$ V) and (-3.0 V/$+3.3$ V) were applied to the WO_3 electrode. For both cases, the voltage is referenced to Pt, and the durations of the coloration and bleaching voltages are 10 and 25 s, respectively. Among the six films with τ_a's of 100–300 °C, the one with $\tau_a = 300$ °C exhibits obvious distinguishing coloration/bleaching responses (Fig. 12) which are surely due to the textured and impermeable oxide network. By applying a small voltage of -2.2 V, the film with $\tau_a = 300$ °C shows only a weak coloration with $\Delta OD \approx 0.025$, but by adjusting the coloration voltage to -3.0 V, its coloration could be remarkably augmented to $\Delta OD \approx 0.25$. This clearly demonstrates that there is a certain threshold barrier of Li^+ intercalation for the highly crystalline film which is consistent with the interpretation of the cyclic voltammograms. The other films exhibited rather similar coloration behavior with respect to each other but the bleaching process of each film was gradually retarded along with the rise of τ_a. For the extreme case of $\tau_a = 300$ °C, the initial colorless states could not be recovered by the present bleaching voltages but require a surplus discharge step which is typically galvanostatic oxidation using a low current density.

The chronoamperometric analysis, which was performed simultaneously with the ΔOD measurement, showed that the ΔOD value of WO_3 film is in rough agreement with the amount of intercalated Li^+ ion. As shown in Fig. 13, the films with lower τ_a exhibit faster electrochemical responses to the voltage switching similar to the optical ones (Fig. 12). During the 10 seconds application of coloration voltage, the total reduction charge was largest in the films with $\tau_a \leqslant 120$ °C. On the other hand, the Q values for these two films begin to converge, indicating that the charge accumulations are almost saturated. The other films with $\tau_a > 120$ °C show steady progress in the reductive intercalation, and are expected to reach equilibrium (or saturation) after an extended coloration time. From the comparison between Figs. 12 and 13, the electrochromic efficiency ($\eta = -\Delta OD/Q$) of each film could be evaluated for the end-point of coloration voltage (time = 10 s). The coloration efficiency of WO_3 film is known to vary substantially

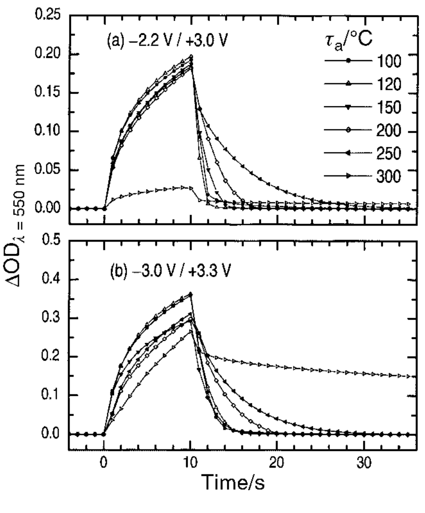

Fig. 12 Optical density change of the WO_3 films during voltage pulses of (a) -2.2 V (10 s)/$+3.0$ V (25 s) and (b) -3.0 V (10 s)/$+3.3$ V (25 s). For both cases the voltages are referenced to Pt.

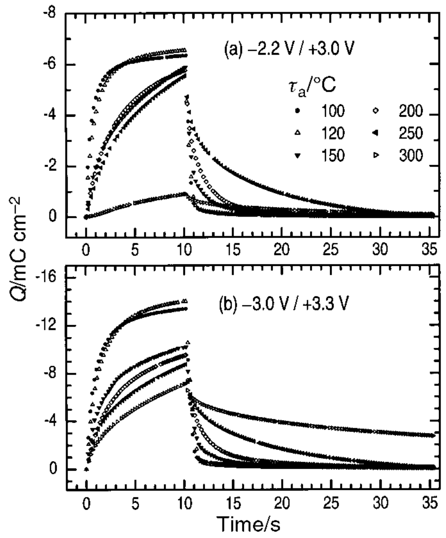

Fig. 13 Charge concentration (Q) in the Li^+ intercalated WO_3 films, evaluated from *in situ* chronoamperometry during the ΔOD measurement in Fig. 12.

depending on the deposition method, and for the sol–gel derived samples, the η value has been reported as 30–40 cm^2 C^{-1}.[33] Also in this study, similar values are observed for all six specimens,[34] where η increases slightly with increasing τ_a. Since the higher electrochromic efficiency is surely attributed to the stronger electronic interaction between intercalated Li^+ ion and WO_3 lattice, we can propose that the Li^+ insertion into the WO_3 film becomes kinetically disfavored but thermodynamically favored as τ_a increases.

From both the cyclic voltammetric analysis and the electrochemioptical property measurements, it was found that Li^+ intercalation into the sol–gel derived WO_3 film is significantly influenced by the annealing temperature. As a general tendency, films treated at lower τ_a show faster Li^+ intercalation/deintercalation kinetics, whereas the Li^+ charge capacity and the host–guest interaction in Li_xWO_3 can be enhanced in films with higher τ_a.

Conclusion

The local structural variation around tungsten in WPA was investigated by temperature-dependent *in-situ* X-ray absorption spectroscopy at the W L_3-edge along with powder XRD, TG/DTA, and FT-IR spectroscopy. The electrochromic property of the WPA based film was also examined for various annealing temperatures between 100–300 °C. The as-prepared WPA xerogel was found to have almost the same structure as that in solution, where the tungstate ions are surrounded by water molecules and hydroxyl groups, and are weakly bound to one another. The temperature-dependent EXAFS/XANES and powder XRD analyses show that WPA undergoes deoxygenation/dehydration (at 20–120 °C) with a gradual formation of linkages between tungstate ions (at 120–350 °C), and eventual crystallization to WO_3 (at $\geqslant$400 °C). Especially at 120–200 °C, which is the optimum heating condition for the electrochromic WO_3 film, WPA contains a significantly developed oxide framework as well as a high level of lithiation sites at the grain surface. It is therefore thought that surface defects like terminal W=O play an important role in the fast diffusion of Li^+ ions, whereas the crystalline domain is also required for reasonable Li^+ capacity.

Acknowledgements

This work was supported in part by the Korea Ministry of Science and Technology through the NRL project, the Korea Ministry of Education through the BK21 program, and the Korea Energy Management Corporation. The authors are also grateful to Dr M. Nomura for help in performing the XAS experiment at PF-KEK.

References

1 T. Nanba, S. Takano, I. Yasui and T. Kudo, *J. Solid State Chem.*, 1991, **90**, 47.

2 J.-H. Choy, Y.-I. Kim, B.-W. Kim, G. Campet, J. Portier and P. V. Huong, *J. Solid State Chem.*, 1999, **142**, 368.

3 J.-H. Choy, Y.-I. Kim, B.-W. Kim, N.-G. Park, G. Campet and J.-C. Grenier, *Chem. Mater.*, 2000, **12**, 2950.

4 J. P. Cronin, D. J. Tarico, J. C. L. Tonazzi, A. Agrawal and S. R. Kennedy, *Sol. Energy Mater. Sol. Cells*, 1993, **29**, 371.

5 C. G. Granqvist, *Handbook of Inorganic Electrochromic Materials*, Elsevier, Amsterdam, 1995, pp. 71–77.

6 F. Di Quarto, G. Russo, C. Sunseri and A. Di Paola, *J. Chem. Soc., Faraday Trans.*, 1982, **78**, 3433.

7 D. G. Barton, M. Shtein, R. D. Wilson, S. L. Soled and E. Iglesia, *J. Phys. Chem. B*, 1999, **103**, 630.

8 R. F. Karlicek, Jr., K. Williams, F. A. Baiocchi, P. M. Thomas and S. Nakahara, *Appl. Phys. Lett.*, 1991, **59**, 2832.

9 K. Yamanaka, H. Okamoto, H. Kidou and T. Kudo, *Jpn. J. Appl. Phys.*, 1986, **25**, 1420.

10 C. Bohnke and O. Bohnke, *J. Appl. Electrochem.*, 1988, **18**, 715.

11 B. Pecquenard, S. Castro-Garcia, J. Livage, P. Y. Zavalij, M. S. Whittingham and R. Thouvenot, *Chem. Mater.*, 1998, **10**, 1882.

12 A. R. West, *Solid State Chemistry and its Applications*, John Wiley & Sons, Singapore, 1989, pp. 90–91.

13 D. E. Sayers and B. A. Bunker, in *X-Ray Absorption; Principles, Applications, Techniques of EXAFS, SEXAFS and XANES*, eds. D. C. Koningsberger and R. Prins, John Wiley & Sons, New York, 1988, pp. 212–253.

14 B. K. Teo, *EXAFS: Basic Principles and Data Analysis*, Springer-Verlag, Berlin, 1986, pp. 114–142.

15 F. W. Lytle, in *Applications of Synchrotron Radiation*, ed. H. Winick, Gordon and Breach, New York, 1989, pp. 135–223.

16 J.-H. Choy, J.-B. Yoon, N.-G. Park, Y.-I. Kim and K.-S. Han, *Jpn. J. Appl. Phys.*, 1997, **36**, 5605.

17 J.-H. Choy, D.-K. Kim, S.-H. Hwang, G. Demazeau and D.-Y. Jung, *J. Am. Chem. Soc.*, 1995, **117**, 8557.

18 M. Newville, P. Livins, Y. Yacoby, J. J. Rehr and E. A. Stern, *Phys. Rev. B: Solid State*, 1993, **47**, 14126.

19 E. A. Stern, *Phys. Rev. B: Solid State*, 1993, **48**, 9825.

20 J. J. Rehr, J. Mustre de Leon, S. I. Zabinsky and R. C. Albers, *J. Am. Chem. Soc.*, 1991, **113**, 5135.

21 J. Mustre de Leon, J. J. Rehr and S. I. Zabinsky, *Phys. Rev. B: Solid State*, 1991, **44**, 4146.

22 P. A. O'Day, J. J. Rehr, S. I. Zabinsky and G. E. Brown, Jr., *J. Am. Chem. Soc.*, 1994, **116**, 2938.

23 B. O. Loopstra and H. M. Rietveld, *Acta Crystallogr., Sect. B*, 1969, **25**, 1420.

24 J. T. Szymanski and A. C. Robert, *Can. Mineral.*, 1984, **22**, 681.

25 E. Salje, *Acta Crystallogr., Sect. B*, 1977, **33**, 574.

26 W. P. Griffith and T. D. Wickins, *J. Chem. Soc. A*, 1968, 397.

27 M. F. Daniel, B. Desbat, J. C. Lassègues, B. Gerand and M. Figlarz, *J. Solid State Chem.*, 1987, **67**, 235.

28 R. A. Nyquist and R. O. Kagel, *Infrared Spectra of Inorganic Compounds (3800–45 cm^{-1})*, Academic Press, San Diego, 1997, pp. 226–227.

29 A. Balerna, E. Bernierni, E. Burattini, A. Kuzmin, A. Lusis, J. Purans and P. Cikmach, *Nucl. Instrum. Methods Phys. Res., Sect. A*, 1991, **308**, 234.

30 F. Hilbrig, H. E. Göbel, H. Knözinger, H. Schmelz and B. Lengeler, *J. Phys. Chem.*, 1991, **95**, 6973.

31 T. Vogt, P. M. Woodward and B. A. Hunter, *J. Solid State Chem.*, 1999, **144**, 209.

32 F. M. Michalak and J. R. Owen, *Solid State Ionics*, 1996, **86**, 965.

33 P. M. S. Monk, R. J. Mortimer and D. R. Rosseinsky, *Electrochromism, Fundamentals and Applications*, VCH, New York, 1995.

34 In the order of $\tau_a = 100$, 120, 150, 200, 250, and 300 °C, $\eta = 30.4$, 30.2, 31.9, 31.7, 33.3, and 30.9 cm^2 °C^{-1}, respectively, for the coloration voltage, −2.2 V, and $\eta = 22.4$, 21.6, 23.9, 26.1, 29.6, and 31.1 cm^2 °C^{-1}, respectively, for −3.0 V.